Variance-reduction kinetic simulation of low-speed rarefied gas flow through long microchannels of annular cross sections

Variance-reduction kinetic simulation of low-speed rarefied gas flow through long micro channels of annular cross sections.

Ferdin Don Bosco[1] and Yonghao Zhang[1, a)]

James Weir Fluids Laboratory, Department of Mechanical and Aerospace Engineering, University of Strathclyde, Glasgow, UK

(Dated: 28 June 2020)

In micro/nano-devices, low-speed transport of mass, momentum, and energy through long-ducts is frequently encountered thereby necessitating scientific investigations. Here, long-ducts of various annular cross-sections conducting low-speed gas flows under the influence of a small pressure gradient are considered, in order to understand how the mass flow rate is affected by rarefaction, variations in radius ratio, and eccentricity of annular geometries. The Boltzmann model equation is treated by a low-variance formulation and simulated by a stochastic kinetic particle-based approach which addresses the deviation of the molecular distribution function from an equilibrium to reduce computational cost significantly. An efficient parallel solver has also been developed and utilized in this research, which is validated against the reported results in the literature. The efficient kinetic particle treatment provides a powerful simulation tool to reveal multi-scale flow physics which is essential to develop and optimise micro/nano-fluidic devices.

[a)]Electronic mail: yonghao.zhang@strath.ac.uk; or y.h.zhang168@gmail.com

I. INTRODUCTION

This paper is dedicated to the memory of Professor Jason M Reese, who had been a true friend, an esteemed mentor, and an inspiration to the authors.

The recent development of a plethora of micro/nano-fluidic applications such as micro/nano-electronic cooling[1], fuel cell technology[2], medical and biomedical devices[3] has attracted significant research interests in micro/nano flows. One of the most prolific process is the gaseous transport through long micro-ducts connecting the various sub-systems. The length of the long micro-duct isolates the end effects to a small region in the immediate vicinity of the reservoirs. Additionally, the length causes the vast portion of the duct to exhibit a nearly constant pressure gradient, irrespective of the pressure difference at the ends, thereby fostering a steady state flow. However, such simplifications do not diminish the importance of understanding of the rich physics associated with the low-signal, rarefied nature of the gas flow, and the small scale of the duct.

Experimental investigations[4–6] have shown that the flows through these micro-ducts exhibit rarefied gas behaviour and the Navier-Stokes model needs to be augmented by the slip velocity boundary condition[7]. Many researchers have focussed on the slip flow regime through micro-ducts[8–10] with various cross-section shapes (channels and circular tubes[11], annular and rectangular shapes[12], and elliptical cross sections[13,14]). Although attempts have been made in extending the slip boundary condition to the second-order based on experimental data[15–17], limited success has been achieved largely due to the inability to reach a consensus regarding the second-order slip coefficient[18]. Even worse, many micro/nano flows are often in the transition flow regime and, sometimes, in the free molecular regime, thus calling for a more fundamental treatment.

The Boltzmann equation provides a robust description of the flow at all rarefaction conditions. Recently, rapid advances have been made in numerical solutions of the Boltzmann equation and its kinetic models for single- and multi-species gas flows[19–24]. Gas flow through various cross sections have been studied such as rectangular[25–30], elliptical[25,31–34], triangular[35,36], trapezoidal[30,36], and concentric annulus[37,38].

The most widely-used and successful computational method for rarefied gas flows is the direct simulation Monte Carlo (DSMC) method[39]. However, it suffers the high degree of statistical uncertainty of the averaged hydrodynamic field variables in low-speed flows with low signal-to-noise ratio[40]. The statistical uncertainty can be reduced by an increase in the number of samples or a reduction in the variance. The former results in expensive computation whereas, the latter approach

is aptly termed as variance reduction methods which can significantly improve computational efficiency.

Recently, the idea of controlling the statistical uncertainty through the incorporation of variance reduction techniques was introduced[41,42] with further improvement for a more efficient calculation of the hard sphere[43,44], variable hard sphere[45], and the relaxation time approximation[46] forms of the collision integral. Other improvements such as using importance weights of the particles to facilitate the retention of DSMC as a special case[47] and the replacement of the Bhatnagar-Gross-Krook (BGK) collision operator by the McCormack kinetic model, thereby enabling the simulation of a binary gas system[48], were also investigated. Although the method has been successfully deployed to study body-force representation of pressure gradients[49], small-scale heat transfer applications[50], second-order temperature jump[51], and multi-scale effects[52], an immense potential remains largely unexplored.

In the present work, a parallel implementation of this method is developed and utilized to study low pressure-gradient driven flows through annular long micro-ducts. The simplicity of the current problem due to its isothermal restriction makes the BGK implementation sufficient. The focus on annular cross-section is primarily due to their numerous peculiar facets. And the investigations into them are sparse. Secondly, these cross-sections possess two independent surfaces that exhibit differing slip characteristics in their vicinity in spite of possessing identical accommodation coefficient. Furthermore, most studies are content to assume full accommodation despite the tangential momentum co-efficient (α) never truly being unity[53]. Lastly, the introduction of an eccentricity in the location of the central cylinder leads to the presence of differing regions of rarefaction requiring a multi-scale approach which is rich in flow physics: a challenge that is uniquely handled by this method.

The paper is organized as below. The second section presents the theoretical principles behind the variance-reduced formulation, introduces the method along with a brief overview of the various operations of the solver, highlights the features that make it uniquely suited to resolve multi-scale flows, and describes the expected outputs and the non-dimensional formulation. The third section establishes the statement of the problem including the different variations considered in this research. The fourth section presents the results and discussion with emphasis on the effect of the variation in flow area, eccentricity, and surface accommodation on mass flow rate. The final section concludes the paper by highlighting the key insights gleaned from this study.

II. VARIANCE REDUCTION METHOD

A. Governing equation

The Boltzmann equation is the foundation of the kinetic theory of gases and is used to describe rarefied gas flows. The equation is of the form,

$$\frac{\partial f}{\partial t} + \mathbf{c} \cdot \frac{\partial f}{\partial \mathbf{r}} + \mathbf{F} \cdot \frac{\partial f}{\partial \mathbf{c}} = \left(\frac{\partial f}{\partial t} \right)_{coll}, \tag{1}$$

where, $f = f(\mathbf{r}, \mathbf{c}, t)$ is the single particle distribution function, $\mathbf{r}$ is the spatial coordinates, $\mathbf{c}$ is the molecular velocity, $\mathbf{F}$ is the force per unit mass, and t is the time. The left and right sides of the equation represent the change in f due to the movement and collision of the molecules respectively.

In addition to retaining and reflecting the key qualitative features of the Boltzmann equation, the BGK model equation also offers intrinsic advantages such as simplification of the complex integro-differential collision term, which provides insights into the inherent gas dynamics through the interpretation of the collision term as a relaxation of the distribution function to an equilibrium state over a time τ_r effectuated by the underlying mechanisms of collisions, i.e.

$$\frac{\partial f}{\partial t} + \mathbf{c} \cdot \frac{\partial f}{\partial \mathbf{r}} + \mathbf{F} \cdot \frac{\partial f}{\partial \mathbf{c}} = \frac{f^{loc} - f}{\tau_r}, \tag{2}$$

where, f^{loc} is the instantaneous local equilibrium distribution function given as

$$f^{loc} = n^{loc} (\sqrt{\pi} v_{mp}^{loc})^{-3} exp \left[- \frac{\left\| \mathbf{c} - \mathbf{u}^{loc} \right\|^2}{{v_{mp}^{loc}}^2} \right], \tag{3}$$

where, n^{loc}, $\mathbf{u}^{loc}$, T^{loc}, and $v_{mp}^{loc} = \sqrt{\frac{2K_b T^{loc}}{m}}$ are the number density, bulk velocity, temperature, and most probable speed at local equilibrium condition respectively and $K_b = 1.380649X10^{-23} J/K$ is the Boltzmann constant[54].

The idea adopted in the current work is to decompose the distribution function into two components: one representing an equilibrium state and the other capturing the deviation (f_d) i.e.

$$f = f_{eq} + f_d, \tag{4}$$

where,

$$f_{eq} = f_0 = f^{mb} = \frac{\rho^{mb}}{{v_{mp}^{mb}}^3 \pi^{\frac{3}{2}}} exp \left(- \frac{\left\| \mathbf{c} - \mathbf{u}^{mb} \right\|^2}{{v_{mp}^{mb}}^2} \right), \tag{5}$$

and

$$f_d(\mathbf{c}) = mW_{eff} \sum_{i=1}^{N} s_i \delta^3(\mathbf{x} - \mathbf{x}_i)\delta^3(\mathbf{c} - \mathbf{c}_i), \tag{6}$$

where, n^{mb}, $\mathbf{u}^{mb}$, and v_{mp}^{mb} are the number density, bulk velocity, and most probable speed at the global equilibrium,f_0, s_i indicates that sign of the particle and is either $+1$ or -1, W_{eff} represents the number of physical particles per simulated particle in addition to the unit deviation represented by the particle.

While it has been established[55] that the spatially variable equilibrium, $f_{eq}(\mathbf{x}, \mathbf{c})$, is considerably more efficient, this efficiency is lost when multiple spatial dimensions are considered. Since such multi-spatial dimensional cases are the focus in this current research, the global equilibrium f_0 is adopted in this work. The solution of the equilibrium part is done analytically and thus, should be analytically solvable making the Maxwell-Boltzmann distribution (see Eq. (5)) an ideal candidate in this work. f_d is the deviation from an equilibrium distribution function and is not a probability distribution function as is evident from the fact that it is neither positive everywhere in the phase space nor is it necessarily normalized or continuous. This makes an analytical evaluation of f_d impossible and the integration of f_d is done through particle representation (see Eq. (6)).

The sign of f_d can vary depending on f and f_{eq} leading to the generated particles possessing either a positive or negative sign. A positive particle indicates that the f is greater than f_{eq} in that phase space element and vice versa. This stipulates that if an equal number of positive and negative particles occupy the same phase space element, then the net change to the distribution function is zero. The number of particles required is dependent on the choice of f_{eq} and ideally, a selection such that $f_d \sim 0$ is highly recommended.

The sole source of non-equilibrium that drives the system away from the global equilibrium in this study is the small, locally constant pressure gradient, which can be represented as a body force in accordance with the precedent established by Cercignani and Daneri in 1963[56]. Consequently, the effect of this body force is an increase in the deviation from equilibrium represented as,

$$\left[\frac{\partial f_d(\mathbf{c})}{\partial t}\right]_{BF} = c_{r_i}\left[\kappa_P + \left(\frac{5}{2} - \frac{\|\mathbf{c} - \mathbf{u}_0\|^2}{v_{mp,0}^2}\right)\kappa_T\right] f_0(\mathbf{c}), \tag{7}$$

where, r_i is the direction and can be x, y or z, c_{r_i} is the molecular velocity in the direction of the body force, $\kappa_P = \frac{L_0}{P_0}\frac{\mathrm{d}P}{\mathrm{d}r_i}$ and $\kappa_T = \frac{L_0}{T_0}\frac{\mathrm{d}P}{\mathrm{d}r_i}$ are the normalized, non-dimensional pressure gradient and temperature gradient in the direction r_i respectively. Here, L_0 is the reference length of the flow.

Under the distribution function decomposition (Eq. (4)) and the body force representation (Eq.

(7)), the governing equation (Eq. (2)) can be recast as

$$\left[\frac{\partial f_d(\mathbf{c})}{\partial t}+\mathbf{c}\cdot\frac{\partial f_d(\mathbf{c})}{\partial \mathbf{r}}\right]+\left[\frac{\partial f_d}{\partial t}\right]_{BF} = \frac{1}{\tau_r}\left[f^{loc}(\mathbf{c})-f_0(\mathbf{c})\right]-\frac{1}{\tau_r}f_d(\mathbf{c}). \tag{8}$$

B. Methodology

The method emulates the DSMC's idea of operator splitting which is valid provided that the chosen time step, Δt, satisfies the condition $\Delta t < t_{mct}$ (mean collision time). Thus, the evolution of the system of signed deviation particles in a single time step, Δt, is governed by

$$Advection\ Operator: \left[\frac{\partial f_d(\mathbf{c})}{\partial t}+\mathbf{c}\cdot\frac{\partial f_d(\mathbf{c})}{\partial \mathbf{r}}\right]\Delta t = 0, \tag{9}$$

$$Collision\ Operator: \left[\frac{\partial f_d(\mathbf{c})}{\partial t}\right]_{coll}\Delta t = \frac{\Delta t}{\tau_r}\left[f^{loc}(\mathbf{c})-f_0(\mathbf{c})\right]-\frac{\Delta t}{\tau_r}f_d(\mathbf{c}), \tag{10}$$

$$Body\ Force: \left[\frac{\partial f_d(\mathbf{c})}{\partial t}\right]_{BF}\Delta t = c_{r_i}\left[\kappa_P+\left(\frac{5}{2}-\frac{\|\mathbf{c}-\mathbf{u}_0\|^2}{v_{mp,0}^2}\right)\kappa_T\right]f_0\Delta t. \tag{11}$$

In the first part of the advection routine, the focus is on the movement of particles which is achieved *a la* DSMC. The advection operator is numerically integrated through updates to the particle's position as

$$r_i(t+\Delta t) = r_i(t)+c_i(t)\Delta t_{adv}, \quad i \in N_{particles}. \tag{12}$$

The second part is the interaction with surfaces and domain boundaries. A particle interacting with a surface can be subject to a diffuse reflection with a probability of α or a specular reflection with the remaining probability $1-\alpha$. Physically, the specular reflection can either represent a smooth, polished wall or a symmetry boundary condition. Diffuse reflection is based on the complete accommodation of the particle to the wall and thus, the particle is re-emitted from the intersection point with velocity sampled from the Maxwellian distribution of the wall temperature. In addition to this, the diffuse surfaces also function as a way of keeping the particle population tractable by deleting oppositely signed particles interacting with the same surface within the time step Δt_{adv}. This implementation is firmly founded on the condition that the surface elements are

small enough that the oppositely signed particle are essentially colliding at the same physical location. The particle's location in velocity space is irrelevant since they are re-sampled from the wall distribution. Thus, the oppositely signed particles are in the same phase space element and their net effect is zero. Periodic boundary conditions are implemented in opposite side pairs of the domain by re-inserting a particle exiting through one boundary through its pair with no change to its velocity.

The BGK collision term integrated over the phase space, i.e. the physical space of cell i represented by D_i and the velocity space represented by R, over a time step, Δt, can be written as,

$$\begin{aligned}
&\int_{D_i}\int_R \left[\frac{\partial f_d(\mathbf{c})}{\partial t}\right]_{coll} \Delta t d^3\mathbf{r} d^3\mathbf{c} \\
&= \int_R \left[\frac{\Delta t \Delta V_i}{\tau_r}\left[f^{loc}(\mathbf{c}) - f_0(\mathbf{c})\right]\right] d^3\mathbf{c} - \int_R \left[\frac{\Delta t \Delta V_i}{\tau_r} f_d(\mathbf{c})\right] d^3\mathbf{c}; \\
&since \int_{D_i} d^3\mathbf{r} = \Delta V_i; \\
&= \int_R \frac{\Delta t \Delta V_i}{\tau_r} \rho_i^{loc} F_i^{loc} d^3\mathbf{c} - \int_R \left[\frac{\Delta t \Delta V_i}{\tau_r} f_d(\mathbf{c})\right] d^3\mathbf{c},
\end{aligned} \tag{13}$$

where, the first term (source) can be implemented in the cell i by generating particles to resolve the difference between the instantaneous local distribution function f^{loc} and established global equilibrium distribution function f_0 while, the second term (sink) is implemented through the removal of deviational particles. The distribution from which the particles are sampled is shown below,

$$\boxed{\left[F_i^{loc} = \frac{1}{\rho_i^{loc}}\left[f_i^{loc}(\mathbf{c}) - f_0(\mathbf{c})\right]\right]_{i\in cell}}. \tag{14}$$

The BGK collision process is formulated in terms of Markov creation and deletion events, N_{events}, where each event, termed as a collision event, occurs during a stochastic sub-time step $t_{c,j}$ with $j = 1, ..., N_{events}$. In a given collision step, the number of collision events continue until the sum of the stochastic sub-time steps exceed the collision time step, i.e. $\sum_{j=1}^{N_{events}} t_{c,j} \geq \Delta t_{coll}$.

The creation or deletion of a particle in the cell i during a collision event affects the instantaneous equilibrium, f^{loc}, and impacts the evaluation of sources and sinks in the subsequent collision event in that cell. It is thus, pivotal to maintain an up-to-date value of the state properties in each cell which can be done by tracking the evolution of the departure from equilibrium state properties. The departure in n^{loc}, $\mathbf{u}^{loc}$ and c^{loc} in a cell j containing N_j particles is given by, $\sum_{i\in N_j} s_i$, $\sum_{i\in N_j} s_i \mathbf{c}_i$, and $\sum_{i\in N_j} s_i \mathbf{c}_i^2$ respectively. The use of instantaneous moments ensures the implementation is devoid of any time step error. Mass conservation is enforced by regenerating the particles

created in the collision step with appropriate signs to make the mass deficit approach zero (see Appendix B).

While the DSMC processes collisions in every cell, the present instance calls for a more nuanced approach in which an appropriate number of collision events are conducted in a few selected cells that contribute towards the system's return to equilibrium.

The determination of the cell and number of collision events (and ergo, size of the stochastic collision sub-time steps) are dependent on the local properties of the cell defined through $(n,u,c)^{loc}_{cell\,i}$. These are obtained through the computation of the upper bound on the absolute integral of equation BGK collision term over the entire phase space shown as,

$$\begin{aligned}
&\int_D\int_R \left[\frac{\partial f_d(\mathbf{c})}{\partial t}\right]_{coll} d^3\mathbf{r}d^3\mathbf{c} \\
&\xrightarrow[Bound]{Upper} \int_D\int_R \left[\frac{\left|f^{loc}(\mathbf{c})-f_0(\mathbf{c})\right|}{\tau_r}+\frac{|f_d(\mathbf{c})|}{\tau_r}\right] d^3\mathbf{r}d^3\mathbf{c} \\
&=\sum_{i=1}^{N_{cell}}\frac{\Delta V_i}{\tau_i}\int_R\left[\left|f^{loc}(\mathbf{c})-f_0(\mathbf{c})\right|+|f_d(\mathbf{c})|\right] d^3\mathbf{c} \\
&=\sum_{i=1}^{N_{cell}}\frac{1}{\tau_i}(B_i^{loc}+N_i^c)=\Lambda,
\end{aligned} \tag{15}$$

where, $B_i^{loc}=\int_R \Delta V_i \left|\left[f^{loc}(\mathbf{c})-f_0(\mathbf{c})\right]\right| d^3\mathbf{c}$ and $N_i^c=\int_R \Delta V_i\,|f_d(\mathbf{c})|\,d^3\mathbf{c}=\sum_{i=1}^{N_p}|s_i|$. The parameter τ_i is the relaxation time based on the local properties defined for cell i and relates directly to the local rarefaction condition of the cell; a high local Kn corresponds to a large relaxation time. In the current process, the sequence of Markov creation and deletion events are carried out with time steps $t_{c,j}$ drawn from the exponential distribution $\Lambda e^{-\Lambda\Delta t_{coll}}$. The time step parameter Λ is indicative of the rate at which trial creation and deletion events are performed and plays a pivotal role in the candidacy determination of cell i. The cell is chosen if it passes the acceptance-rejection test which takes into account the local state through the numerator of Eq. (16) and τ_i.

$$P_i^{cell}=\frac{B_i^{loc}+N_i^c}{(B_i^{loc}+N_i^c)_{max}}=\frac{B_i^{loc}+N_i^c}{\Lambda\tau_i}. \tag{16}$$

Once the cell and stochastic time step have been determined, the particle creation steps are processed with probability $\frac{B_i^{loc}}{B_i^{loc}+N_i^c}$, and random particles are removed from cell i with the remaining probability. The process is clarified in the flowchart presented in Fig. 1.

The body force term and its integration are resolved by drawing particles from the distribution

F_{BF}, i.e.

$$\left[\frac{\partial f_d}{\partial t}\right]_{BF} = c_{r_i}\left[\kappa_P + \left(\frac{5}{2} - \frac{\|\mathbf{c}-\mathbf{u}_0\|^2}{v_{mp,0}^2}\right)\kappa_T\right] f_0, \tag{17}$$

$$\int_D\int_R \left[\frac{\partial f_d}{\partial t}\right]_{BF} \Delta t d^3\mathbf{r} d^3\mathbf{c} = \int_R \frac{\rho_0 v_{mp,0}}{L} F_{BF} V_{ps} \Delta t d^3\mathbf{c}, \tag{18}$$

where,

$$V_{ps} = \int_D d^3\mathbf{r}, \tag{19}$$

and

$$\boxed{F_{BF} = \frac{v_{mp,0}^2 L}{\rho_0} c_{r_i}\left[\kappa_P + \left(\frac{5}{2} - \frac{\|\mathbf{c}-\mathbf{u}_0\|^2}{v_{mp,0}^2}\right)\kappa_T\right] f_0}. \tag{20}$$

The total number of particles that need to be created to represent the effect of the body force is determined through the integration of the upper bound of Eq. (20). The drawing of the particles must be performed in a mass conservative manner through the creation of an equal number of positive and negative particles. This is achieved through stratified sampling of F_{BF}.

During each time step, the advection, collision and the effect of the body force are implemented as elaborated above. The convergence condition is monitored and once it has been achieved, the sampling operation is incorporated into the process. The operator splitting, borrowed from DSMC, often leads to a time step error, which is mitigated here by utilizing Strang's splitting method[57] to achieve second-order convergence with no intrinsic time step error.

The current procedure executes the following algorithm during a single time step:

1. Half execution of body force ($\Delta t_{BF} = 0.5 \times \Delta t$);
2. Half execution of Advection ($\Delta t_{adv} = 0.5 \times \Delta t$);
3. Full execution of Collision ($\Delta t_{coll} = \Delta t$);
4. Half execution of Advection ($\Delta t_{adv} = 0.5 \times \Delta t$);
5. Half execution of body force ($\Delta t_{BF} = 0.5 \times \Delta t$);
6. Sample properties.

The evaluation of the hydrodynamic properties is computed along a similar vein as in the DSMC method albeit, the summation of the deviational particles corresponds to the difference

between the steady-state values and the equilibrium. The determination of the hydrodynamic properties for density, bulk velocity and pressure tensor are shown below,

$$\rho_j = \rho_0 + \frac{nW_{eff}}{\Delta V_j} \sum_{i \in N_j} s_i, \tag{21}$$

$$\rho_j \mathbf{u}_j = \rho_0 \mathbf{u}_0 + \frac{nW_{eff}}{\Delta V_j} \sum_{i \in N_j} s_i c_i, \tag{22}$$

$$\mathbf{P}_j + \rho_j \mathbf{u}_j \mathbf{u}_j = \mathbf{P}_0 + \rho_0 \mathbf{u}_0 \mathbf{u}_0 + \frac{nW_{eff}}{\Delta V_j} \sum_{i \in N_j} s_i c_i c_j. \tag{23}$$

More detailed description of the above method can be obtained from Radtke and Hadjiconstaninou[46]. The entire process is depicted pictorially in the flowchart (Fig. 1) below.

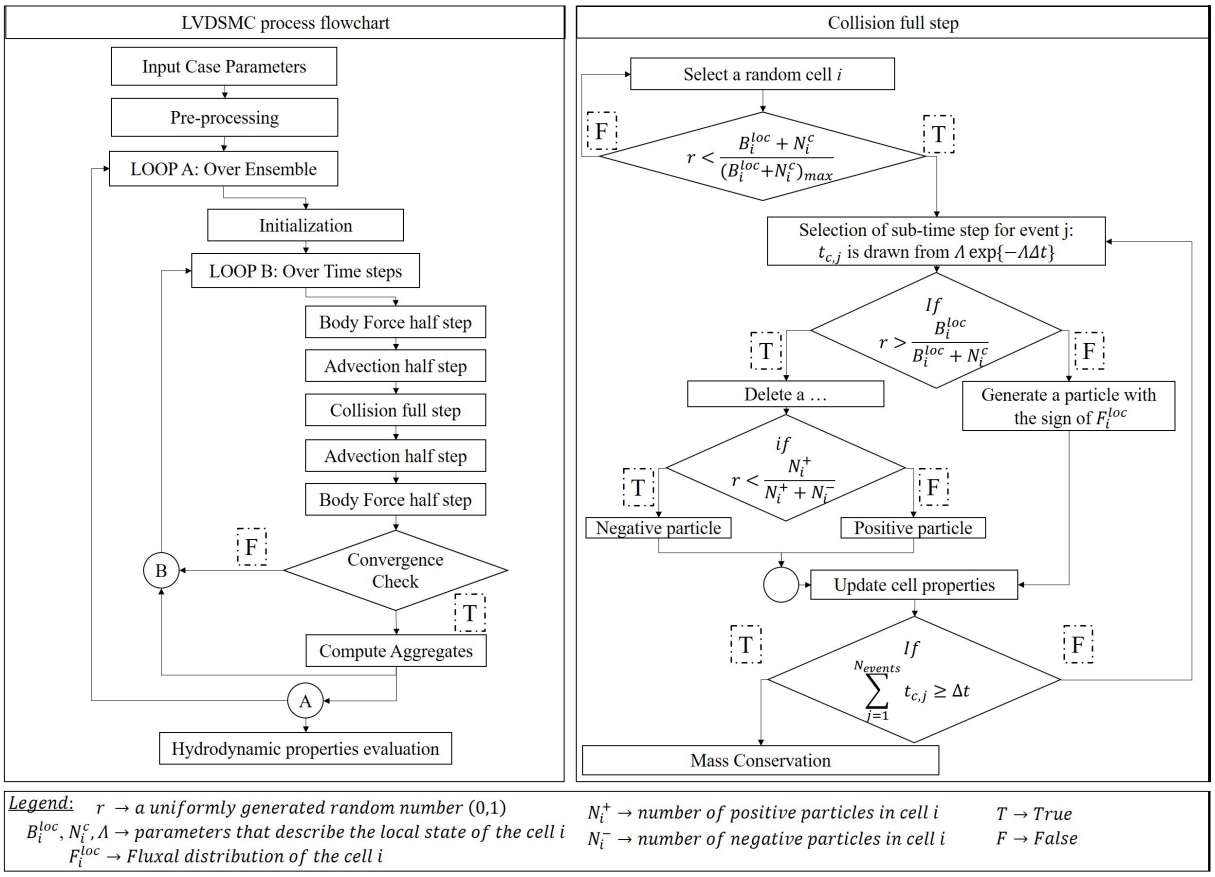

FIG. 1: Flowchart of the main process of the method with a focus on the collision process.

C. Features

A unique vantage point that is afforded by the particulate nature of the current method is the ability to track the number of particles colliding with a unit elementary surface. Thus, for every

impact on surface k, the parameter $Agg\ SI$ is updated as,

$$(Agg\ SI)_k = (Agg\ SI)_k + 1. \tag{24}$$

The time-averaged version of this value signifies the effect that the surface had in the relaxation to an equilibrium of the system. Termed as surface interactivity, a high value indicates that the surface is significantly involved in the development of the flow characteristics while a low value means that the surface plays a negligible role.

The selection of a cell is dependent on the cell's relaxation time τ_i (see Eq. (16)) which is inversely related to the cell's number density (implying that it is directly related to the local Knudsen number). Once selected, the determination of the number of collision events in a cell during a time step, Δt_{coll}, is dependent on the collision sub-step which in turn depends on the instantaneous state of that cell.

This is where the ingenuity of the present implementation and its natural ability to adapt to a multi-scale system is evidenced. To exemplify the adaptation to multi-scale effects, consider that a cell in the region of high local rarefaction is chosen first. Then the time taken for the first collision event $t_{c,1}$ will be long and very few other collisions can occur in the remaining portion of the time step Δt_{coll}. On the other hand, if the cell is chosen from a region of low local rarefaction, then the time taken for this first collision event $t_{c,1}$ will be short and several subsequent collision events can occur in the remaining portion of the time step Δt_{coll}. This implies that a low rarefaction region will be collision dominated whereas a high rarefaction region will be dominated by advection.

D. Formulation of non-dimensional quantities

The low-signal nature of the flows result in a small difference between the measured quantities and their reference value, and small values of pressure gradients and velocity need to be scaled up to avoid computational errors. This is achieved by using ε which can be chosen such that it normalizes the largest source of non-equilibrium. At present, the flows are induced by a small and constant pressure gradient along a direction (say, z) in which case the the non-dimensional form of the gradient ($\hat{\kappa_p}$) can be expressed as,

$$\hat{\kappa_p} = \frac{L_0}{P_0 \varepsilon} \frac{\mathrm{d}P}{\mathrm{d}z} = 1. \tag{25}$$

Here, the spatial coordinates of the phase space are made dimensionless by defining a length L_0 termed as the characteristic length of the flow domain whereas, the velocity space is made non-dimensional with respect to the most probable speed of the molecules occupying the phase space represented by $v_{mp,0}$ and is a function of the temperature and type of gas. The hydrodynamic state variables namely, number density n, temperature T and pressure P are made non-dimensional with respect to a reference state defined by a reference number density n_0, temperature T_0 and pressure P_0 respectively. The non-dimensional parameters in the present work are represented by a caret ($\hat{}$) or a subscript $_{ND}$ as below,

$$\begin{gathered} x_{ND} = \hat{x} = \frac{x}{L_0}; \quad y_{ND} = \hat{y} = \frac{y}{L_0}; \quad z_{ND} = \hat{z} = \frac{z}{L_0}; \\ u_{ND} = \hat{u} = \frac{u}{\varepsilon v_{mp,0}}; \quad v_{ND} = \hat{v} = \frac{v}{\varepsilon v_{mp,0}}; \quad w_{ND} = \hat{w} = \frac{w}{\varepsilon v_{mp,0}}; \\ n_{ND} = \hat{n} = \frac{n}{n_0}; \quad T_{ND} = \hat{T} = \frac{T}{T_0}; \quad P_{ND} = \hat{P} = \frac{P}{P_0}; \\ t_{ND} = \hat{t} = \frac{L_0 t}{v_{mp,0}}; \quad f_{ND} = \hat{f} = \frac{v_{mp,0}^3}{n_0} f. \end{gathered} \tag{26}$$

For annular cross sections with inner and outer diameters D_i and D_o, the reference length is considered to be the hydraulic diameter calculated as,

$$D_h = D_o - D_i = L_0. \tag{27}$$

The corresponding form of the governing equation is given by,

$$Kn_{scaled}\left(\frac{\partial \hat{f}}{\partial \hat{t}} + \hat{\mathbf{c}} \cdot \frac{\partial \hat{f}}{\partial \hat{\mathbf{r}}} + \hat{c}_z \hat{\kappa}_P \hat{f}_0\right) = \frac{\hat{f^{eq}} - \hat{f}'}{\hat{\tau}_r} \tag{28}$$

where,

$$Kn_{scaled} = \frac{v_{mp,0}\tau_0}{L_0}. \tag{29}$$

Introducing $\bar{c} = \sqrt{\frac{8K_bT}{\pi m}}$ as the mean molecular speed, the equation for Kn_{scaled} then becomes

$$Kn_{scaled} = \left(\frac{v_{mp,0}}{\bar{c}}\right)\frac{\tau_0 \bar{c}}{L_0} = \frac{\sqrt{\pi}}{2}\frac{\lambda}{L_0} = \frac{\sqrt{\pi}}{2}Kn, \tag{30}$$

where, τ_0 is the relaxation time of the reference state, $\lambda = \tau_0 \bar{c}$ is the mean free path of the gas, and $Kn = \frac{\lambda}{L_0}$ is the global Knudsen number.

In the low Kn_{scaled} cases, the effect of the streaming operator (left side of Eq. (28)) is diminished and the flow is collision dominated whereas, high Kn_{scaled} values will tend to make the

collision operator (right side of Eq. (28)) insignificant thereby establishing a ballistic dominated flows with an extreme case of free molecular flows. Moreover, the degree of rarefaction of the flow is often represented by the scaled rarefaction parameter that is related to the Knudsen number as

$$\delta_{scaled} = \frac{2}{\sqrt{\pi}} \frac{1}{Kn} = \frac{1}{Kn_{scaled}}. \tag{31}$$

The important flow characteristics such as mass transport and friction characteristics are expressed as the reduced mass flow rate (G_p) and the Poiseuille number (Po), respectively. A simplified expression for the Poiseuille number for the long micro-duct was obtained from kinetic considerations[58] and is used in the related study. These parameters are expressed as,

$$G_p = 2\dot{m}_{ND} = 2 \int \int n_{ND} u_{ND} dA_{ND}, \tag{32}$$

$$Po = \frac{8\tau_w D_h}{\mu_0 u_{\bar{ND}}} = \frac{\pi}{2} \frac{\delta_{scaled}}{u_{\bar{ND}}}, \tag{33}$$

where, G_p is normalized by $\frac{P_0}{v_{mp,0}}$. Finally, the contour plot of a hydrodynamic property for multiple Knudsen numbers are often presented together. This juxtaposition is more amenable to comprehension if each of the cases is normalized with respect to its local maximum value. For example, we represent the velocity magnitude $|V|$ by the local maximum normalized scaled speed (V_{max}) defined as,

$$V_{max} = \frac{|V|}{Max(|V|)}; |V| = \sqrt{u_{ND}^2 + v_{ND}^2 + w_{ND}^2}. \tag{34}$$

III. FLOW CONFIGURATION AND COMPUTATIONAL PARAMETERS

Consider two reservoirs, R_1 and R_2 containing a monoatomic gas at states P_1, T_1 and P_2, T_2 respectively with $P_1 > P_2$. The length, L, of the interconnecting micro-duct is such that it can be considered as a long micro-duct with wall temperature, T_w, fulfilling the condition, $T_1 = T_2 = T_w = T = constant$. The statement of the problem considering a substantial gradient only in the flow direction (z-direction) can be concisely conveyed through Fig. 2.

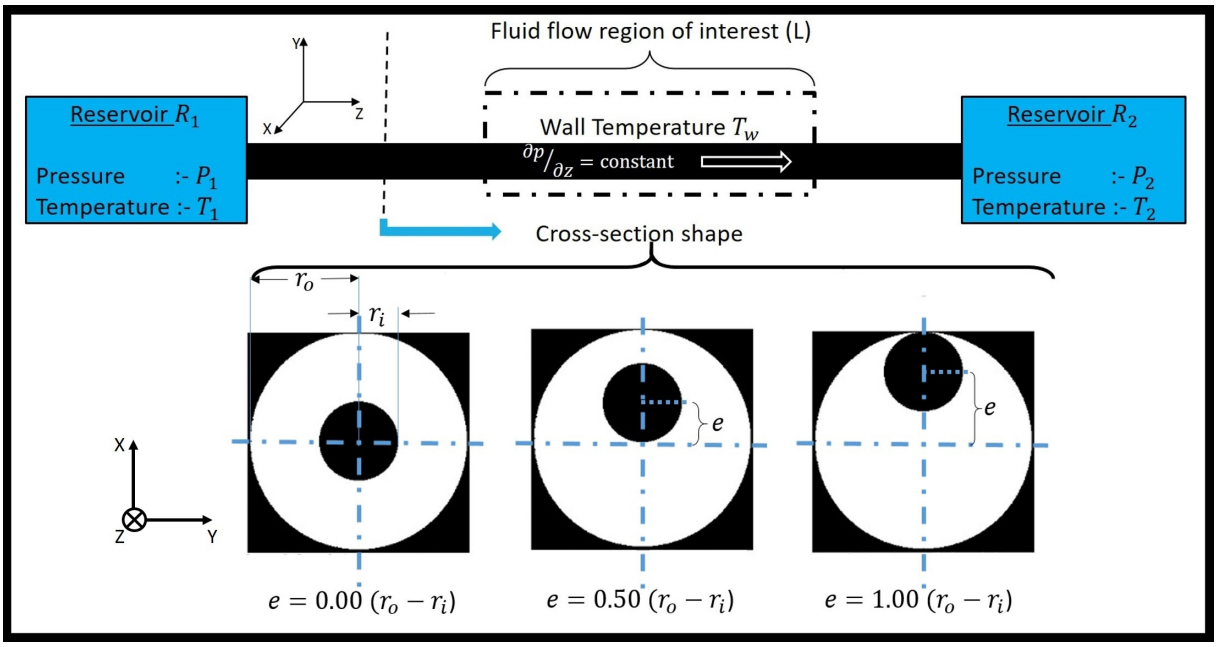

FIG. 2: Schematic diagram depicting the flow configuration through annular long micro-ducts.

Properties associated with the outer cylinder is marked with the subscript $_o$ and the inner cylinder is marked with the subscript $_i$. The purpose of this study is to discern and characterize the effect of flow area which is varied by changing the inner cylinder radius (r_i) as shown in Tab. I.

TABLE I: Annular cross sections considered in this study and their associated tags.

Tag	Radius ratio (r_i/r_o)
Annulus A	0.20
Annulus B	0.35
Annulus C	0.50
Annulus D	0.60
Annulus E	0.80

Additionally, the eccentricity (e) is also varied as 0%, 25%, 50%, 75%, and 100% of the gap, $(r_o - r_i)$. Concentric annuli are a special case where the eccentricity is 0%. The effect of surface accommodation coefficient is investigated by considering various values of the inner and outer cylinder's accommodation coefficients (denoted by α_i and α_o). Further inspection of the surface effect on flow is achieved through the differential variation of α_i and α_o. In the first instance α_o is maintained at 1.00 while, α_i assumes values of $(0.90, 0.80, 0.70)$ in separate cases. In the second

instance, α_o is varied as $(0.90, 0.80, 0.70)$ while, α_i is kept constant as 1.00.

IV. RESULTS AND DISCUSSIONS

In long ducts, the transport of mass is a balance between bulk transport, which is caused by the inertial core of flow, and surface transport, which occurs due to velocity slip and Knudsen diffusion. In the continuum regime (low Knudsen numbers), the bulk transport dominates the overall transport whereas, an increase in rarefaction is indicative of the increase in the surface transport. The Knudsen minimum is typically observed in the transitional regime in the vicinity of $Kn = 1.00$. While this phenomenon is prominently featured in the present studies of annular sections, the focus here is to characterize the behaviour of the flow when subject to the aforementioned structural variations.

A. Effect of cross-section area

Although the method has been previously validated for different flows including pressure-driven plane Poiseuille flows[49], the second-order temperature jump[51] and study of a Knudsen compressor[52], we first compare our simulation results with the data reported in Breyiannis *et. al.*[37], where discrete velocity method (DVM) was used to solve the BGK equation.

The consideration is restricted to concentric ($e = 0\%$) annuli with equal inner and outer surface accommodation coefficient ($\alpha_i = \alpha_o$). Various annular sections are considered through the increase of radius ratio which results in decreasing flow area while also increasing the proximity of the inner and outer surfaces.

The very low slip velocity in continuum flows can lead to high frictional effects, characterized by the Poiseuille number, which is a strong function of the cross-section area resulting in a large spread for the various annular sections in the continuum regime (inset of Fig. 3b). Conversely, the frictional effects is weaker (*Po* number is small) in the rarefied regime and a closer spread of the Poiseuille number across different annular sections is observed (see Fig. 3b).

Similarly, the mass flow rate in the rarefied regime is primarily due to surface transport which is facilitated by the low friction effects (as indicated by the low *Po* number) and is strongly dependent on the surface area leading to a larger spread in the mass flow rate of the different annuli in the rarefied regime (see inset "a" of Fig. 3a). As the continuum regime is reached, the surface

transport diminishes as the friction effects increases (as indicated by the high *Po* number) and the bulk transport dominates the flow. Under these conditions a larger surface area is detrimental as evidenced by Fig. 3a. The Knudsen minimum is also clearly observed in Fig. 3a.

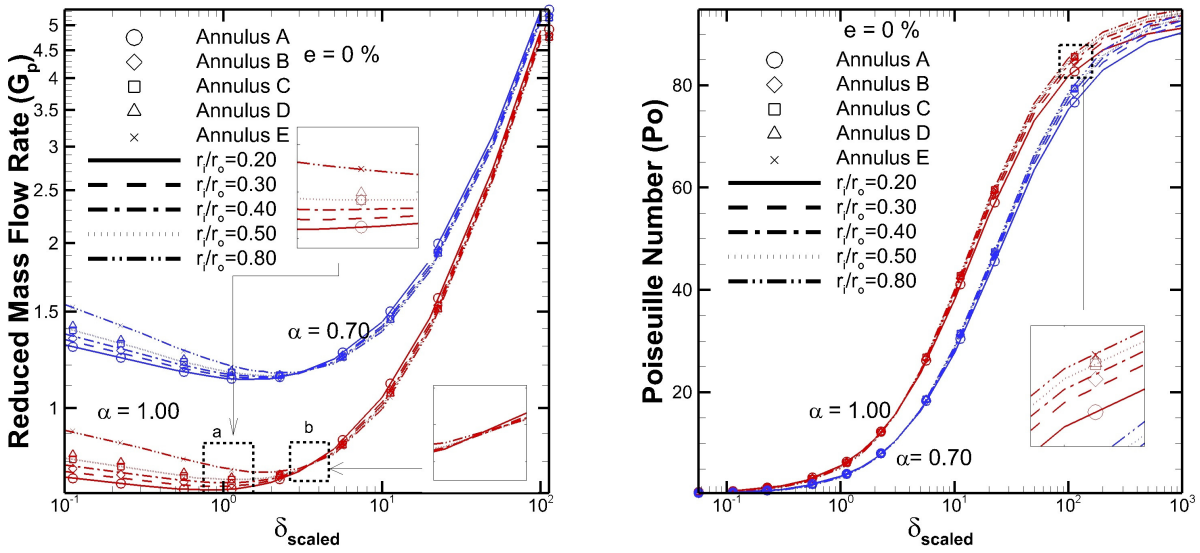

(a) Reduced mass flow rate.

(b) Poiseuille number.

FIG. 3: Variations in Flow Area (r_{ratio}) for the annular cross section long micro-duct. The present results are denoted by symbols and compared with the DVM results[37] denoted by lines. The results for $\alpha = 1.00$ are indicated by the red lines whereas the results for $\alpha = 0.70$ are indicated by the blue lines.

From the V_{max} contours (Fig. 4), it can be inferred that the peak velocity occurs in the vicinity of the gap's centreline whereas the surfaces are subject to slip. The effect of increasing surface accommodation coefficient, α, is to decrease the slip velocity, whereas, an increase in rarefaction results in a larger slip velocity and a flatter velocity profile (Fig. 5).

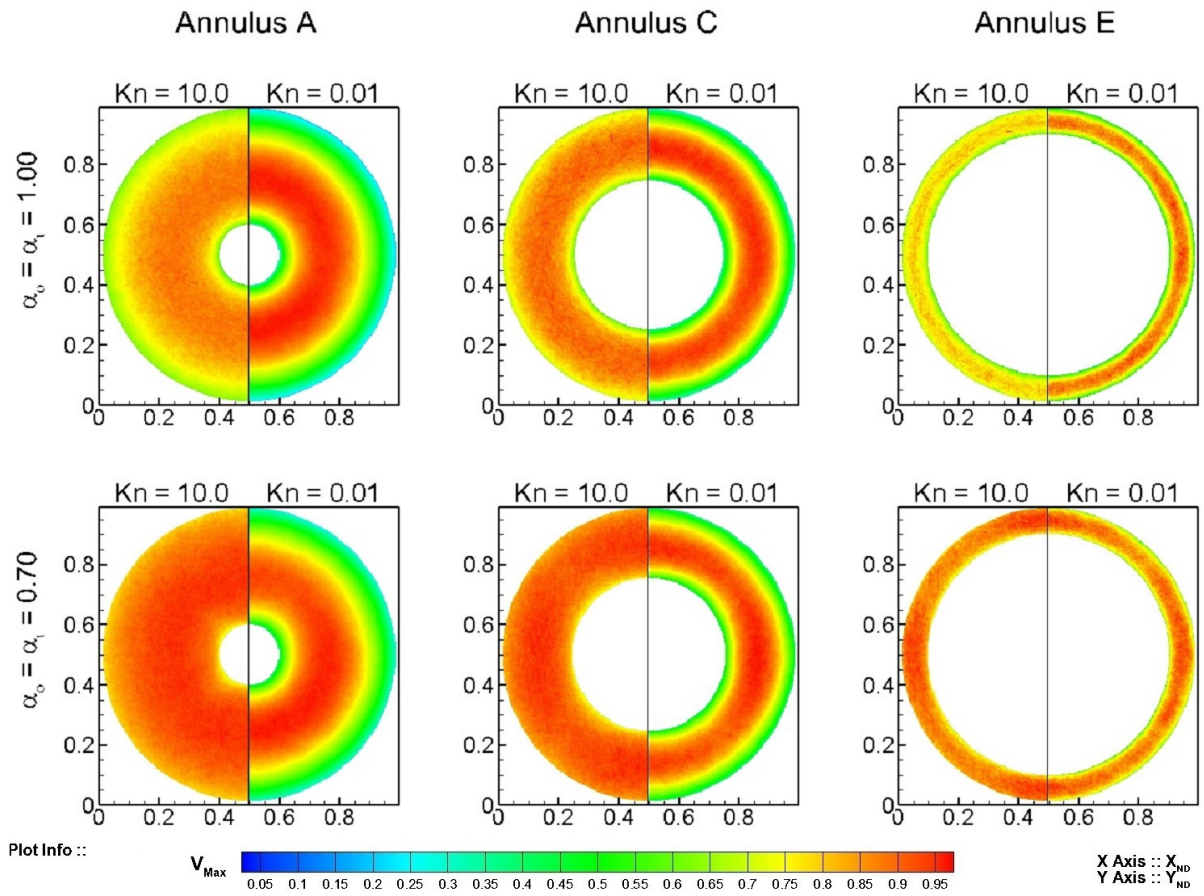

FIG. 4: V_{max} contour with varying r_{ratio} for the long micro-ducts with annular cross sections.

An additional observation afforded by the velocity profiles (Fig. 5) is the unequal slip characteristics at the inner and outer surfaces at all the Knudsen numbers despite having the same accommodation coefficient. The inner surface is observed to exhibit a higher slip velocity which results in a shift in the peak velocity towards the inner surface. The effect is more pronounced in lower radius ratios, such as Annulus A, where the surfaces are further apart. This is due to relatively higher rarefaction in the flow field close to the inner surface where the local characteristic length scale of the flow is smaller. As the radius ratio increases, the two surfaces draw closer and the difference in rarefaction between the two surfaces becomes insignificant resulting in similar slip and more asymmetrical velocity profile.

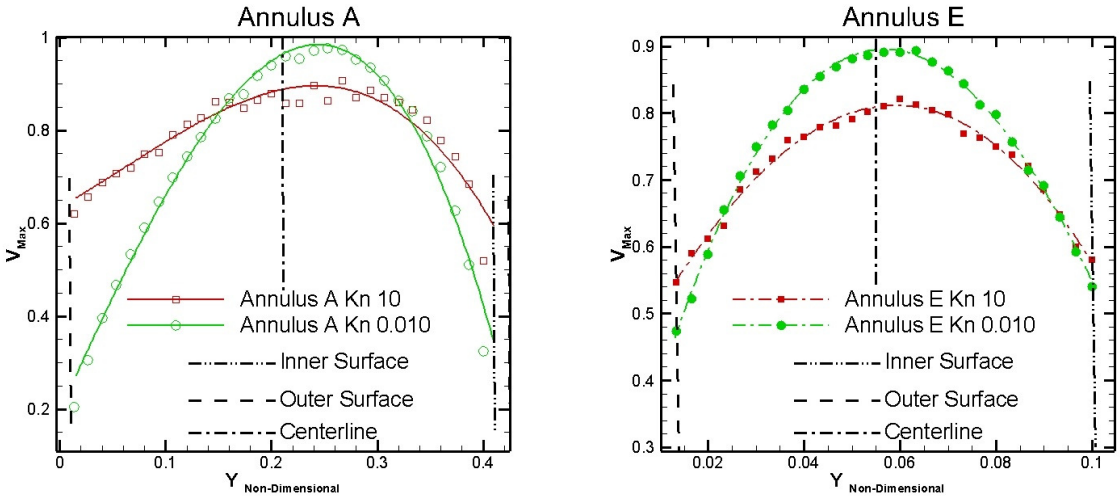

FIG. 5: V_{max} profile at $X = 0.50$: Annulus A ($r_{ratio} = 0.2$) and Annulus E ($r_{ratio} = 0.8$). The lines are a second-order fit to the data points denoted by the symbols.

Fig.3a and Fig.3b show excellent agreement with the DVM results reported by Breyiannis *et. al.*[37], which confirms the validity of the present method and implementation. Hereafter, we focus on how flow is affected by geometries, rarefaction and surface/gas interactions.

B. Effect of eccentricity

We now investigate the effect of eccentricity by varying the location of the inner cylinder with unity tangential momentum accommodation coefficient at the inner and outer surfaces ($\alpha_i = \alpha_o = 1.00$).

The V_{max} contours for these geometries highlight the effect of flow rarefaction as the inner cylinder approaches the outer surface. The feature of such a geometric design is the separation of the flow field into a relatively unrestricted flow regime below the inner cylinder (the area "a" in Fig. 6) that is more conducive to bulk transport and a highly restricted flow region dependent on surface transport above the inner cylinder (the area "b" in Fig. 6). The "b" area is locally more rarefied than the "a" area, resulting in a multi-scale flow. The present method is suitable to simulate multi-scale flows, which is discussed in more details in Appendix A.

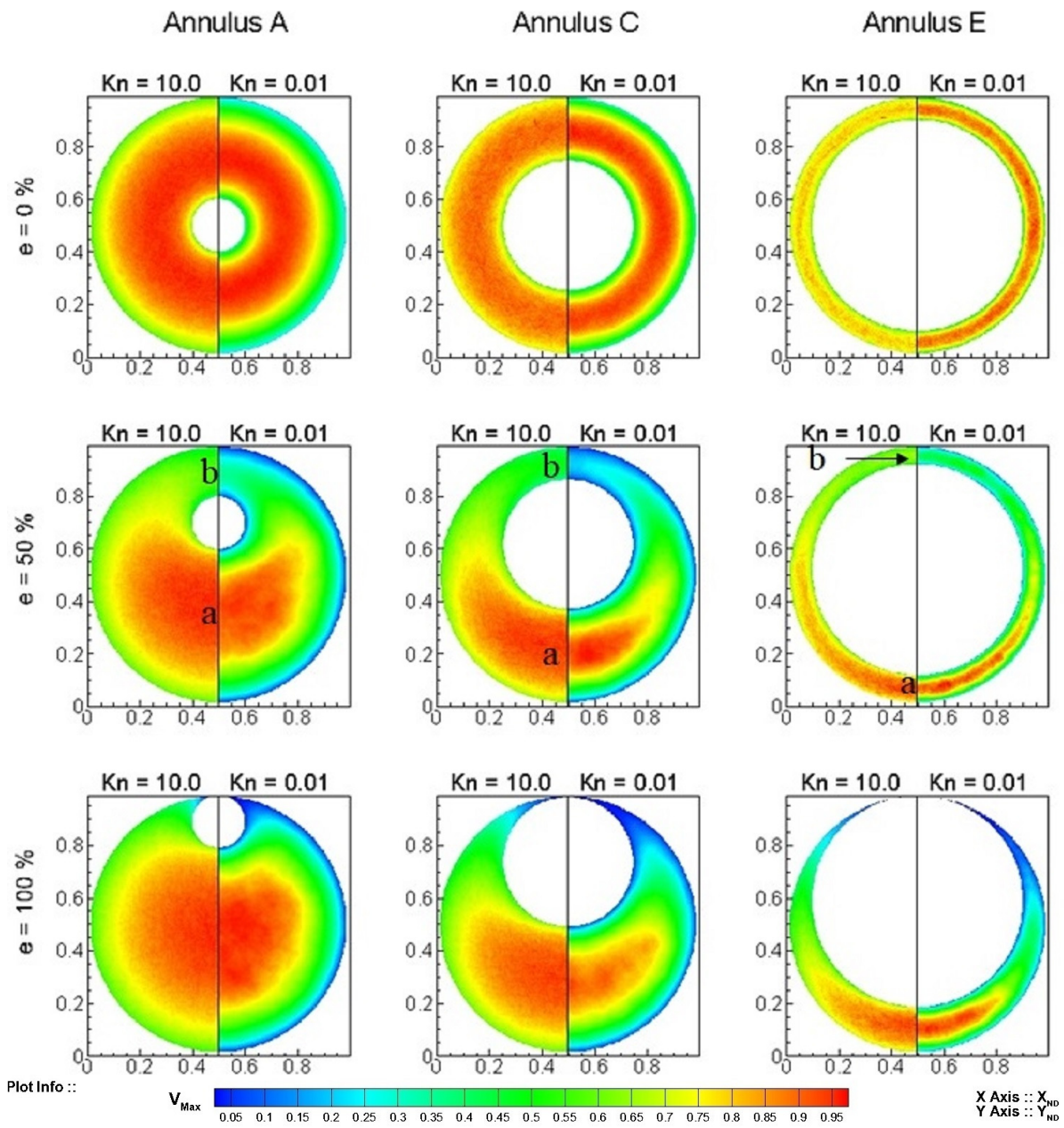

FIG. 6: V_{max} contour for varying eccentricity and radius ratio.

The effect of the geometry on the mass flow rate can be discussed from two congruent standpoints to draw attention to the various features of the flow through eccentric annular cross-sections.

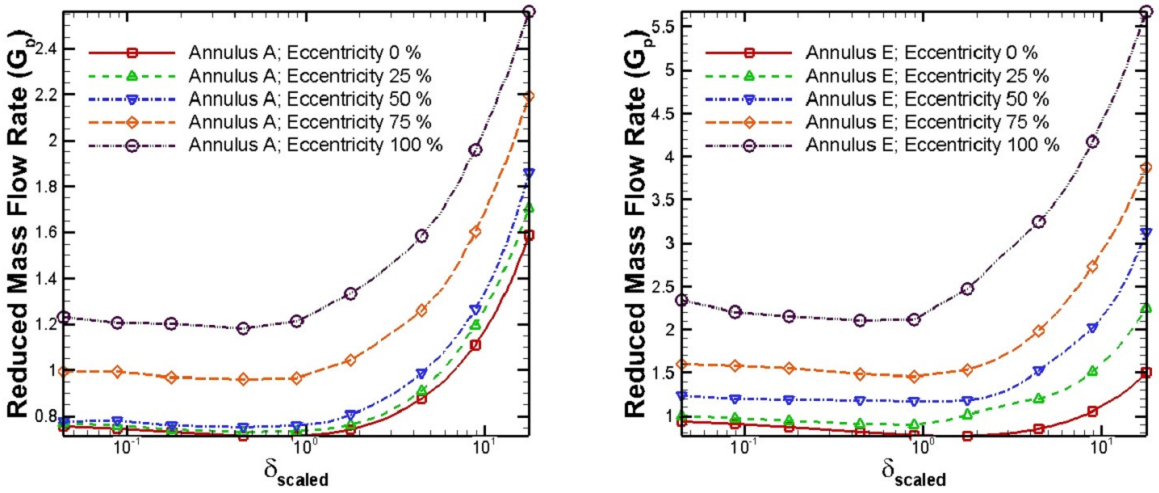

FIG. 7: Reduced mass flow rate for varying eccentricity.

The displacement of the inner cylinder from its central axis causes inhomogeneous slip at both inner and outer cylinder surfaces resulting in flow features that do not reciprocate the behaviour of the concentric annular cases. The increase in eccentricity for a particular annular cross section is accompanied by an increase in the mass flow rate at all the Knudsen numbers (Fig. 7). This observation is explained by recalling that a shift in the inner cylinder causes the flow to be more conducive in one portion of the flow area while the other is less conducive to flows. At higher eccentricities, the flow in the area "b" becomes more rarefied and the transport in the area "a" is enhanced. For a given eccentricity, the composition of the areas "a" and "b" is different for different radius ratios, thus, at a specified eccentricity the Annulus E fosters a higher mass flow rate than Annulus A (Fig. 8).

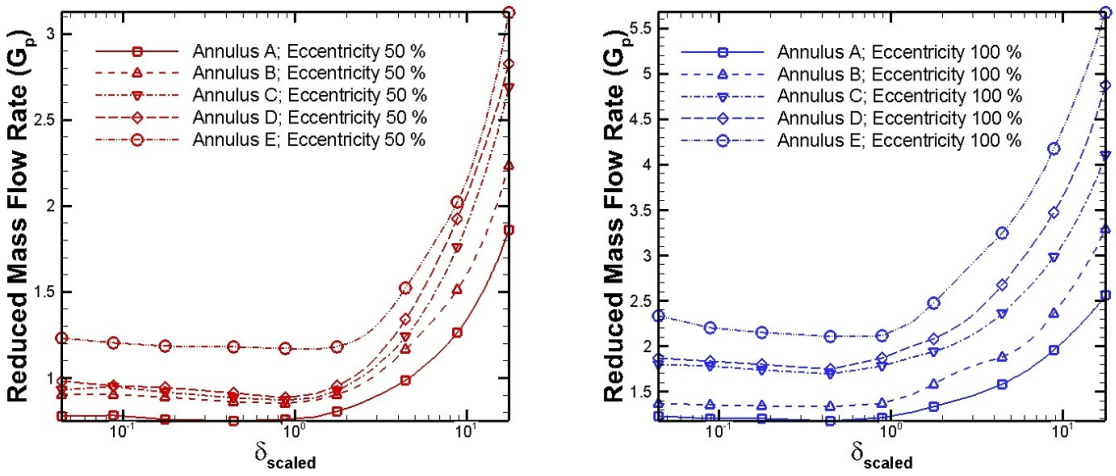

FIG. 8: Reduced mass flow rate for the specific eccentricities (50% and 100%) as the radius ratio varies.

In a concentric annulus, the central location of the inner cylinder results in every surface element of the inner cylinder exerting an equal influence on the the flow and generating the same slip velocity. As the inner cylinder is displaced towards the outer surface, the portion of the inner cylinder surface in proximity to the outer surface is locally more rarefied (i.e. the area "b"), which does not play a major role in the mass transport. When eccentricity increases, a larger part of the inner cylinder surface plays a less significant role in the mass flow. To elaborate this point, further evidence is provided by plotting the normalized surface interactivity (calculated as per Eq. (24)) of the inner cylinder surface elements for Annulus B at eccentricities of 0% and 50%. The central location of the cylinder with $e = 0\%$ results in every surface interacting equally with the particles which can be interpreted by the equal heights of the blue bars in Fig. 9. The offset of the inner cylinder in $e = 50\%$ and the consequent unsymmetrical flow field about the X axis (as shown in the contours of Fig. 6) cause an imbalance in the interactivity between fluid and the surface elements. The elements receptive to the larger flow area are seen to be more active while their counterparts that are exposed to the smaller flow area are relatively less interactive, which is highlighted for $e = 50\%$ by the red bars in Fig. 9. While the results are presented for $Kn = 1.00$, a similar trend is seen to persist across all the Knudsen numbers, although the difference between the most and least interactive surface elements reduces as the flow becomes rarefied. The maximum eccentricity signifies the position at which the inner cylinder exerts its least influence on the flow field and

thus, such geometries exhibit the maximum mass flow rate as indicated in Fig. 7.

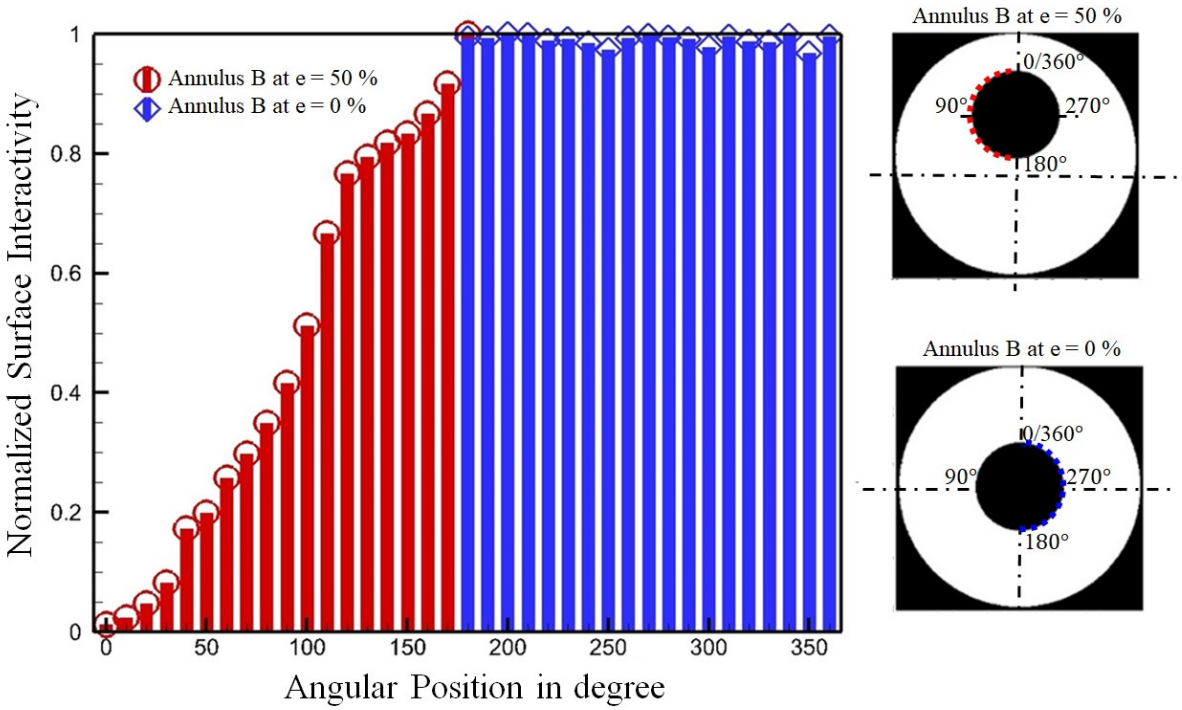

FIG. 9: Comparison of surface interactivity for the internal cylinder surface of Annulus B at eccentricity of 50% and 0%.

C. Effect of surface accommodation coefficient

The effect of surface/gas interactions on flow can be characterized by tangential accommodation coefficient. Here, the considerations extend to the cases where the inner and outer surfaces possess equal ($\alpha_i = \alpha_o$) and unequal ($\alpha_i \neq \alpha_o$) accommodation coefficient. The impetus behind this investigation is that modern precision manufacturing techniques can make highly polished surfaces using materials such as silicon, glass, ceramics, and polymers, which leads to substantial variation of tangential accommodation coefficient. The present study is restricted to concentric annular cases only for purposes of brevity and clarity.

The V_{max} contours at different Kn are presented in Fig. 10 where the left and right halves denote the effect of equal and unequal α respectively. The contours indicate that for equal α values, a smaller α is more favourable to mass flow because of enhanced slip at the surface, which is quantitatively presented in Fig. 11. Another observation gained from the contours is that the

flow field is sensitive to α, and that a smaller α_o hosts a more conducive velocity field than a smaller α_i because of a larger outer surface area.

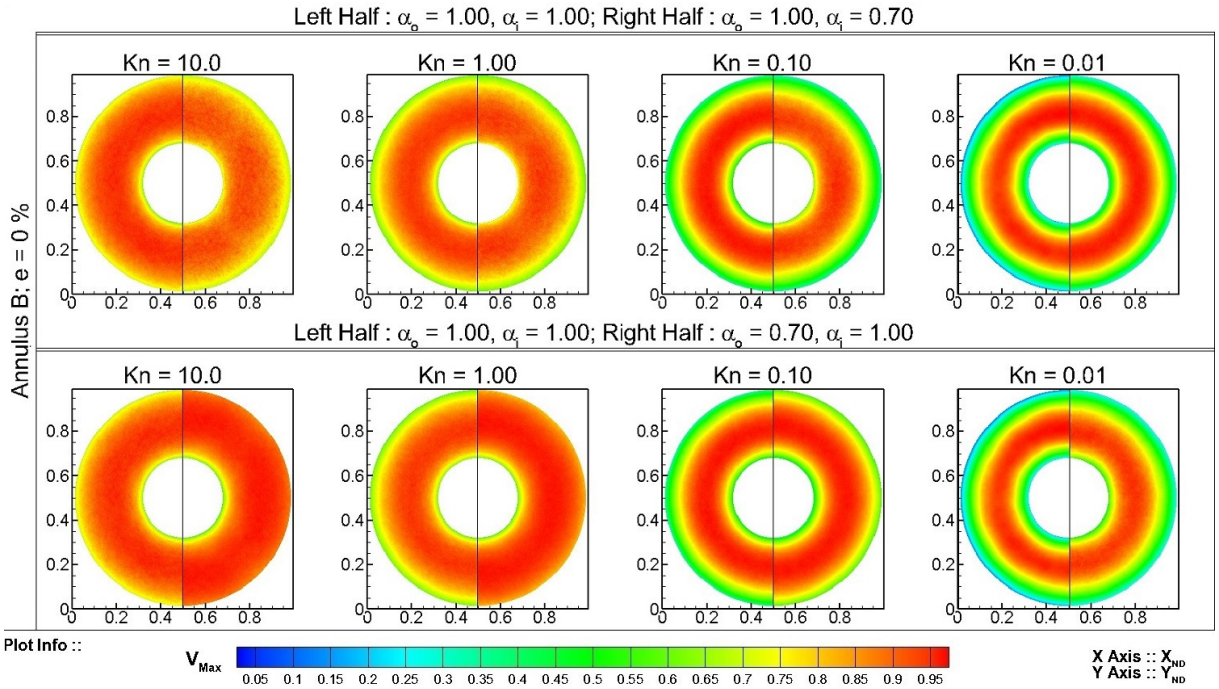

FIG. 10: V_{max} contour for differential α.

Fig. 11 shows, for any given annular cross-section, a smaller outer surface accommodation (α_o) is more productive than a smaller inner surface accommodation (α_i). For instance, the reduced mass flow rate from highest to the lowest is ordered as $(\alpha_i, \alpha_o) = (0.7, 0.7) > (\alpha_i, \alpha_o) = (1.0, 0.7) > (\alpha_i, \alpha_o) = (0.7, 1.0)$. This difference in the mass flow rate in the cases with unequal α is seen to diminish as the radius ratio increases. Finally, the difference becomes small as the flow approaches the continuum regime, as the slip at the surface becomes negligible.

The reduction of α_o increases the slip of the outer surface and contributes to the increased flow rate. This effect is seen to be less noticeable at high radius ratio as the surfaces draw closer. This increase in radius ratio negates the difference in slip (as evidenced by Annulus E in Fig. 5) and thus, at a high radius ratio, the effect of decreasing α_o is comparable to decreasing α_i as indicated by the small difference in the solid and open symbols for Annulus E in Fig. 11c. On the other hand, the effect is more definitively felt at smaller radius ratios such as Annulus A.

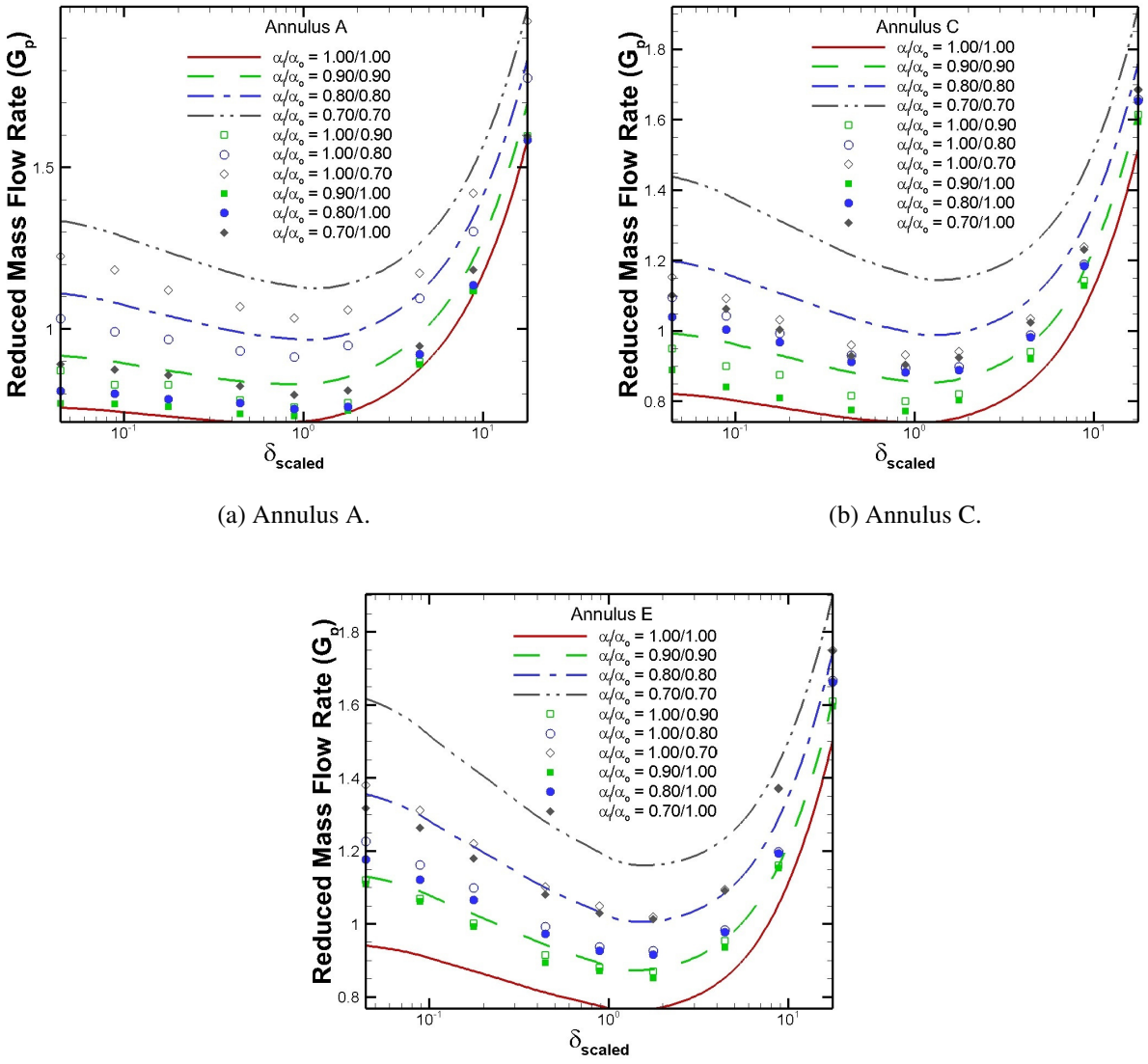

(a) Annulus A.

(b) Annulus C.

(c) Annulus E.

FIG. 11: Reduced mass flow rate at different inner and outer surface accommodation coefficient.

Although the results of the above studies strongly indicate the efficiency of the method, it is limited to applications with small deviations from an underlying equilibrium state. In the low speed flows considered here, the deviation from equilibrium is indeed small for all the Knudsen numbers[59] which enables the application of the present method. As a particle method which is required to keep particle numbers tractable, the present method becomes expensive in the continuum regime due to the dominance of the collision process. Another key consideration is the number of particles per cell. While the present studies have obtained reliable results with 20 particles per

cell, a very low number will lead to high particle weights and could result in non-physical results such as a negative density and temperature.

V. CONCLUDING REMARKS

In the present work, a kinetic particle approach based on the variance reduced form of the Boltzmann-BGK model is employed to investigate the rarefied gas flows through various annular long-ducts prominently featured in micro/nano devices. The present analysis helps to understand the effects of geometry, surface conditions, and rarefaction.

It is observed that the inequality of the inner and outer surface slip characteristics causes a significant number of peculiarities in annular flows, e.g. a high mass flow rate for a large radius ratio is evidenced for rarefied flow. For increasing eccentricity, the flow becomes more multi-scale in nature and the effect of this is seen through enhanced mass flow rate. The inhomogeneous slip at the inner and outer surfaces plays a pivotal role and a decrease in the outer surface's accommodation coefficient relative to the inner surface leads to a more favourable mass flow.

This study has demonstrated the potential of the present method to resolve low-signal, rarefied gas flows, which are commonly found in micro/nano systems and porous media.

ACKNOWLEDGMENTS

We would like to thank our colleagues Dr. Minh Tuan Ho and Dr. Thomas Burel for their insightful comments.

DATA AVAILABILITY STATEMENT

The data that support the findings of this study are available from the corresponding author upon reasonable request.

Appendix A: Multiscale effect

Annulus B is considered to elaborate how the solver treats multiscale flow with locally-varying rarefaction. This is done by identifying two regions of equal size, located half way between the inner and outer cylinder surfaces, namely Region I in the area "a" and Region II in the area "b". The multi-scale nature is quantified by measuring the average size of the collision sub-step. Due

to the reliance of this sub-step on the local instantaneous properties, the value of the average sub-time step in different regions differs significantly. A higher average sub-time step indicates a low number of collision events which is a characteristics of rarefied flows and vice versa. From Fig. 12, $t_{R-I} < t_{R-II}$ indicates that Region II is more rarefied than Region I. The solver resolves this by automatic processing of less collision events in Region II compared to Region I. The relative ratio is seen to increase as the global rarefaction reduces, as shown by the trend presented in the table inset of Fig. 12.

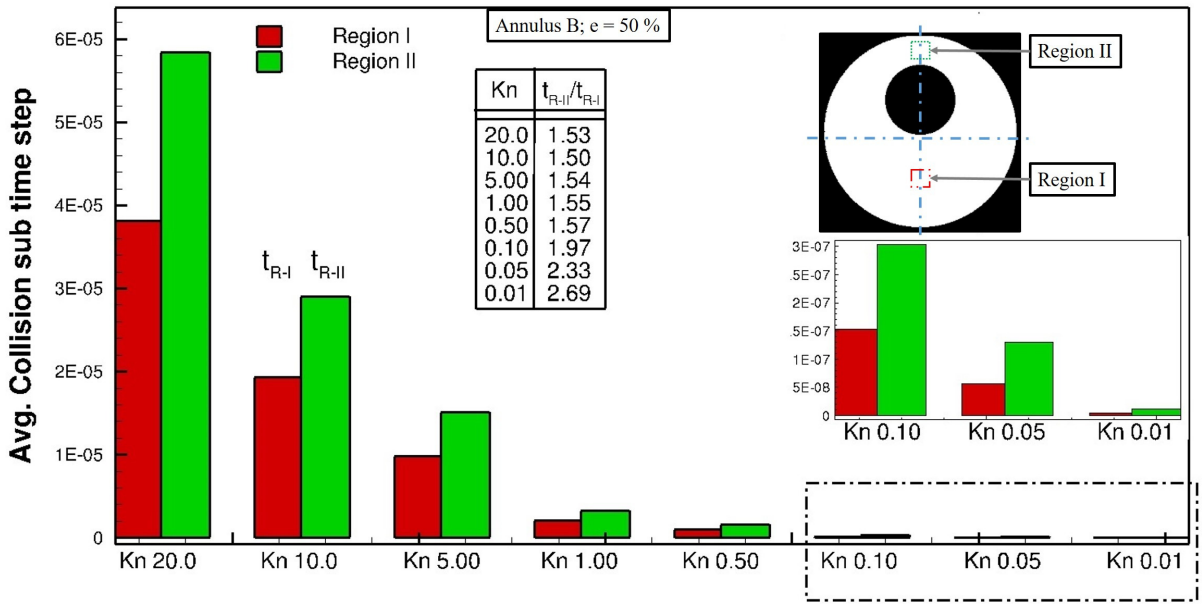

FIG. 12: Multi-scale adaptability for Annulus B at an eccentricity of 50%.

Appendix B: Conservation of Mass, Momentum, and Energy

In DSMC, conservation of mass, momentum and energy is ensured at each collision, whereas the LVDSMC algorithm conserves these quantities on average. The mass conservation is enforced through proper considerations in the particle generation procedure to minimize the mass deficit in each time step.

The mass deficit or mass residual is denoted by ΔS which is defined as the difference in the number of particles created during a generation process. Thus, $\Delta S = N^{+}_{gen} - N^{-}_{gen}$ where, N^{+}_{gen} and N^{-}_{gen} are the number of positive and negative particles generated at that time step. A subsequent generation of a positive particle will change the deficit as $\Delta S = \Delta S + 1$ whereas, the generation of a negative particle will modify the deficit as $\Delta S = \Delta S - 1$. Ideally, for a mass conserved step,

the mass deficit at the end of a time step should be zero ($\Delta S = 0$). In the method outlined in this work, the processes that lead to generation of particles are the implementation of the body force and the collision process. Surface motion and surface temperature will also necessitate generation of particles but are not considered in the present study.

The global nature of the body force encourages the practice of generating an equal number of positive and negative particles (sampled from Eq. (20)) in each half step. This stratified sampling approach ensures that the mass deficit remains zero. The collision process is not global and the sign of the particles generated depends on the local properties of the cell which affect the fluxal distribution given by Eq. (14) from which the particles are generated. It is therefore possible that an unequal number of positive and negative particles are generated in a single collision step. In such cases, corrections are implemented on the particles generated during that step to restore mass conservation ($\Delta S \to 0$). The correction procedure consists of deleting a random and recently generated particle with sign of ΔS and subsequently generating a particle with the sign opposite to ΔS.

If the mass deficit is even, then a parity correction is implemented (see Illustration A in Fig. 13). However, if the deficit is an odd value, then a complete correction is not feasible and the regeneration procedure is applied to attain the minimum ΔS value (see Illustration B in Fig. 13). Alternatively, if the deficit is unity then no correction is applicable (see Illustration C in Fig. 13). Any outstanding deficit is then carried over to the subsequent time step and is addressed as part of that step's correction.

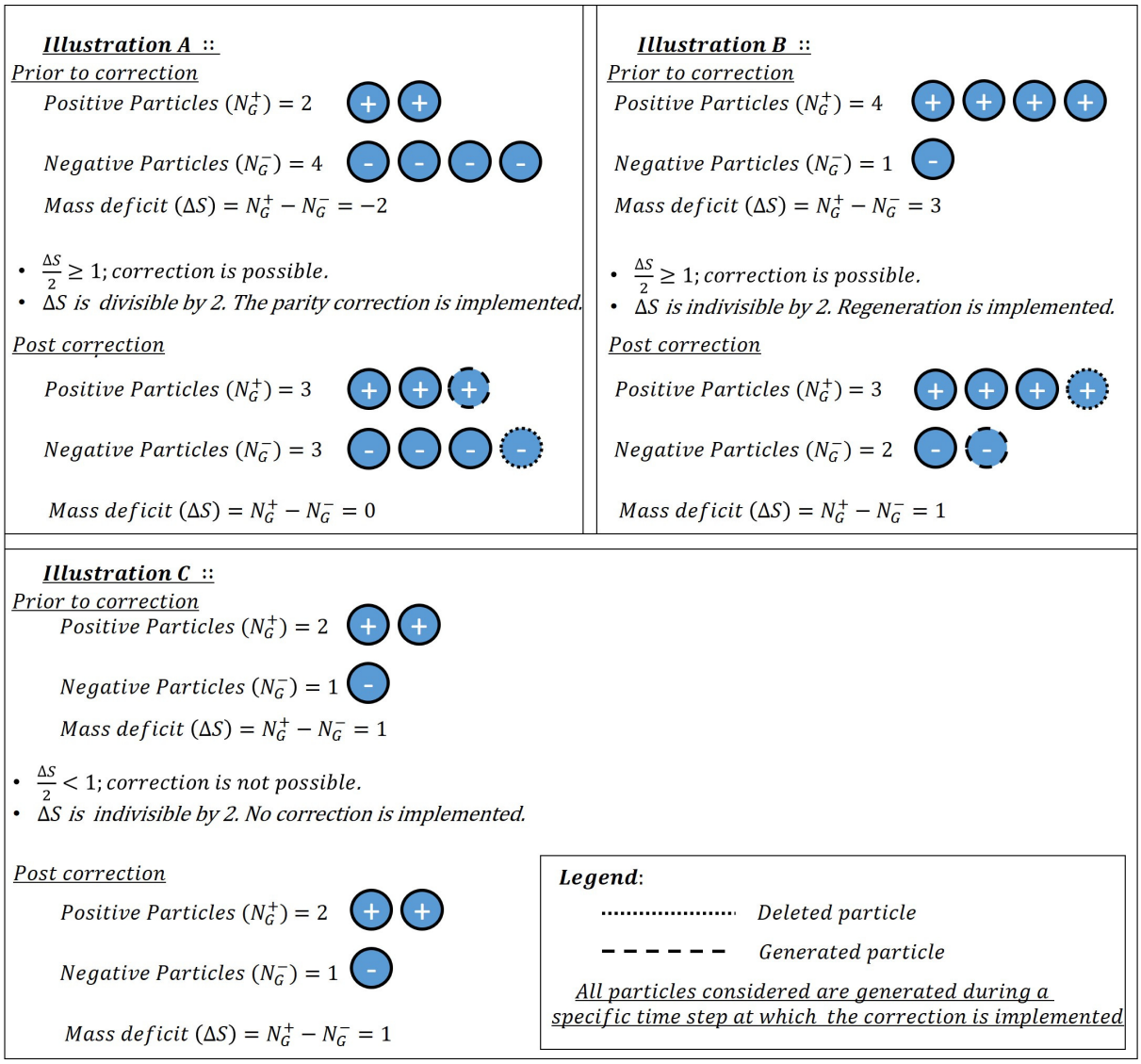

FIG. 13: Illustration of the mass deficit and corrections.

Once the mass conservation is ensured, the conservation of momentum and energy is dependent on the velocities of the signed particles which are appropriately drawn from the fluxal distributions i.e. Eqs. (20) and (14). This ensures that the momentum and energy are conserved on average i.e. stochastically.

REFERENCES

[1]B. Antohe, J. Lage, D. Price, and R. M. Weber, "Numerical characterization of micro heat exchangers using experimentally tested porous aluminum layers," International Journal of Heat

and Fluid Flow **17**, 594–603 (1996).

[2]S. W. Cha, R. O'Hayre, and F. B. Prinz, "The influence of size scale on the performance of fuel cells," Solid State Ionics **175**, 789–795 (2004).

[3]A. A. Merrikh and J. L. Lage, "Effect of blood flow on gas transport in a pulmonary capillary," Journal of biomechanical engineering **127**, 432–439 (2005).

[4]E. B. Arkilic, M. A. Schmidt, and K. S. Breuer, "Gaseous slip flow in long microchannels," Journal of Microelectromechanical systems **6**, 167–178 (1997).

[5]T. Araki, M. S. Kim, H. Iwai, and K. Suzuki, "An experimental investigation of gaseous flow characteristics in microchannels," Microscale Thermophysical Engineering **6**, 117–130 (2002).

[6]J. Maurer, P. Tabeling, P. Joseph, and H. Willaime, "Second-order slip laws in microchannels for Helium and Nitrogen," Physics of Fluids **15**, 2613–2621 (2003).

[7]J. Liu, Y.-C. Tai, and C.-M. H.-C. Pong, "MEMS for pressure distribution studies of gaseous flows in microchannels," in *Micro Electro Mechanical Systems, 1995. IEEE Proceedings* (1995) p. 209.

[8]M. Gad-el Hak, *The MEMS handbook* (CRC press, 2001).

[9]J. C. Harley, Y. Huang, H. H. Bau, and J. N. Zemel, "Gas flow in micro-channels," Journal of Fluid Mechanics **284**, 257–274 (1995).

[10]G. Karniadakis, A. Beskok, and N. Aluru, *Microflows and nanoflows: Fundamentals and simulation*, Vol. 29 (Springer Science & Business Media, 2006).

[11]E. H. Kennard *et al.*, *Kinetic theory of gases, with an introduction to statistical mechanics* (McGraw-Hill, 1938., 1938).

[12]W. Ebert and E. M. Sparrow, "Slip flow in rectangular and annular ducts," Journal of Basic Engineering **87**, 1018–1024 (1965).

[13]Z. Duan and Y. Muzychka, "Slip flow in elliptic microchannels," International Journal of Thermal Sciences **46**, 1104–1111 (2007).

[14]Z. Duan and Y. Muzychka, "Slip flow in non-circular microchannels," Microfluidics and Nanofluidics **3**, 473–484 (2007).

[15]S. Colin, Cécile Aubert, "High-order boundary conditions for gaseous flows in rectangular microducts," Microscale Thermophysical Engineering **5**, 41–54 (2001).

[16]S. Colin, P. Lalonde, and R. Caen, "Validation of a second-order slip flow model in rectangular microchannels," Heat Transfer Engineering **25**, 23–30 (2004).

[17]A. Sreekanth, "Slip flow through long circular tubes," Proceedings of the sixth international

symposium in rarefied gas dynamics **1**, 667–680 (1969).

[18]R. W. Barber and D. R. Emerson, "Challenges in modeling gas-phase flow in microchannels: From slip to transition," Heat Transfer Engineering **27**, 3–12 (2006).

[19]L. Wu, H. Liu, Y. Zhang, and J. Reese, "Influence of intermolecular potentials on rarefied gas flows: Fast spectral solutions of the Boltzmann equation," Physics of Fluids **27**, 082002 (2015).

[20]P. Wang, M. Ho, L. Wu, Z. Guo, and Y. Zhang, "A comparative study of discrete velocity methods for low-speed rarefied gas flows," Computers & Fluids **161**, 33–46 (2018).

[21]M. Ho, L. Zhu, L. Wu, P. Wang, Z. Guo, Z. Li, and Y. Zhang, "A multi-level parallel solver for rarefied gas flows in porous media," Computer Physics Communications **234**, 14–25 (2190).

[22]W. Yang, X. Gu, L. Wu, D. Emerson, and Y. Zhang, "A hybrid approach to couple the discrete velocity method and method of moments for rarefied gas flows," Journal of Computational Physics **410**, 109397 (2020).

[23]X. Zhao, C. Wu, Z. Chen, L. Yang, and C. Shu, "Reduced order modeling-based discrete unified gas kinetic scheme for rarefied gas flows," Physics of Fluids **32**, 067108 (2020).

[24]W. Su, L. Zhu, P. Wang, Y. Zhang, and L. Wu, "Can we find steady-state solutions to multiscale rarefied gas flows within dozens of iterations," Journal of Computational Physics **407**, 109245 (2020).

[25]V. Rykov, V. Titarev, and E. Shakhov, "Rarefied Poiseuille flow in elliptical and rectangular tubes," Fluid Dynamics **46**, 456–466 (2011).

[26]F. Sharipov, "Rarefied gas flow through a long rectangular channel," Journal of Vacuum Science & Technology A: Vacuum, Surfaces, and Films **17**, 3062–3066 (1999).

[27]F. Sharipov, "Non-isothermal gas flow through rectangular microchannels," Journal of Micromechanics and Microengineering **9**, 394 (1999).

[28]I. Graur and M. Ho, "Rarefied gas flow through a long rectangular channel of variable cross section," Vacuum **101**, 328–332 (2014).

[29]V. Titarev and E. Shakhov, "Kinetic analysis of the isothermal flow in a long rectangular microchannel," Computational Mathematics and Mathematical Physics **50**, 1221–1237 (2010).

[30]S. Varoutis and D. Valougeorgis, "Estimation of the Poiseuille number in gas flows through rectangular nano-and micro-channels in the whole range of the Knudsen number," in *IUTAM Symposium on Advances in Micro-and Nanofluidics* (2009) pp. 79–86.

[31]L. Yang, C. Shu, W. Yang, and J. Wu, "An improved three-dimensional implicit discrete velocity method on unstructured meshes for all Knudsen number flows," Journal of Computational

Physics **396**, 738–760 (2019).

[32]V. Titarev, M. Dumbser, and S. Utyuzhnikov, "Construction and comparison of parallel implicit kinetic solvers in three spatial dimensions," Journal of Computational Physics **256**, 17–33 (2014).

[33]I. Graur and F. Sharipov, "Gas flow through an elliptical tube over the whole range of the gas rarefaction," European Journal of Mechanics-B/Fluids **27**, 335–345 (2008).

[34]I. Graur and F. Sharipov, "Non-isothermal flow of rarefied gas through a long pipe with elliptic cross section," Microfluidics and Nanofluidics **6**, 267–275 (2009).

[35]S. Naris, D. Valougeorgis, D. Kalempa, and F. Sharipov, "Flow of gaseous mixtures through rectangular microchannels driven by pressure, temperature, and concentration gradients," Physics of Fluids **17**, 100607 (2005).

[36]S. Varoutis, S. Naris, V. Hauer, C. Day, and D. Valougeorgis, "Computational and experimental study of gas flows through long channels of various cross sections in the whole range of the Knudsen number," Journal of Vacuum Science & Technology A: Vacuum, Surfaces, and Films **27**, 89–100 (2009).

[37]G. Breyiannis, S. Varoutis, and D. Valougeorgis, "Rarefied gas flow in concentric annular tube: Estimation of the Poiseuille number and the exact hydraulic diameter," European Journal of Mechanics-B/Fluids **27**, 609–622 (2008).

[38]N. Dongari, C. White, T. J. Scanlon, Y. Zhang, and J. M. Reese, "Effects of curvature on rarefied gas flows between rotating concentric cylinders," Physics of Fluids **25**, 052003 (2013).

[39]G. A. Bird, *Molecular gas dynamics and the direct simulation of gas flows* (Clarendon, 1994).

[40]Q. He, Q. Wang, X. Wang, and L. Luo, "DSMC simulation of low-speed gas flow and heat transfer in 2D rectangular micro-channel," Progress in Computational Fluid Dynamics **5**, 230–235 (2005).

[41]L. L. Baker and N. G. Hadjiconstantinou, "Variance reduction for Monte Carlo solutions of the Boltzmann equation," Physics of Fluids **17**, 051703 (2005).

[42]L. L. Baker and N. G. Hadjiconstantinou, "Variance reduction in particle methods for solving the Boltzmann equation," in *ASME 4th International Conference on Nanochannels, Microchannels, and Minichannels* (American Society of Mechanical Engineers, 2006) pp. 377–383.

[43]T. M. Homolle and N. G. Hadjiconstantinou, "A low-variance deviational simulation Monte Carlo for the Boltzmann equation," Journal of Computational Physics **226**, 2341–2358 (2007).

[44]T. M. Homolle and N. G. Hadjiconstantinou, "Low-variance deviational simulation Monte

Carlo," Physics of Fluids **19**, 041701 (2007).

[45]G. A. Radtke, N. G. Hadjiconstantinou, and W. Wagner, "Low-noise Monte Carlo simulation of the variable hard sphere gas," Physics of Fluids **23**, 030606 (2011).

[46]G. A. Radtke and N. G. Hadjiconstantinou, "Variance-reduced particle simulation of the Boltzmann transport equation in the relaxation-time approximation," Physical Review E **79**, 056711 (2009).

[47]H. A. Al-Mohssen and N. G. Hadjiconstantinou, "Low-variance direct Monte Carlo simulations using importance weights," ESAIM: Mathematical Modelling and Numerical Analysis **44**, 1069–1083 (2010).

[48]L. Szalmas, "Variance-reduced DSMC for binary gas flows as defined by the McCormack kinetic model," Journal of Computational Physics **231**, 3723–3738 (2012).

[49]M. R. Allshouse and N. G. Hadjiconstantinou, "Low-variance Deviational Monte Carlo simulations of pressure-driven flow in micro-and nanoscale channels," AIP Conference Proceedings **1084**, 1015–1020 (2008).

[50]N. G. Hadjiconstantinou, G. A. Radtke, and L. L. Baker, "On variance-reduced simulations of the Boltzmann transport equation for small-scale heat transfer applications," Journal of Heat Transfer **132**, 112401 (2010).

[51]G. A. Radtke, N. G. Hadjiconstantinou, S. Takata, and K. Aoki, "On the second-order temperature jump coefficient of a dilute gas," Journal of Fluid Mechanics **707**, 331–341 (2012).

[52]G. A. Radtke, J.-P. M. Péraud, and N. G. Hadjiconstantinou, "On efficient simulations of multiscale kinetic transport," Philosophical Transactions of the Royal Society A: Mathematical, Physical and Engineering Sciences **371**, 20120182 (2013).

[53]T. Ewart, P. Perrier, I. A. Graur, and J. G. Méolans, "Mass flow rate measurements in a microchannel, from hydrodynamic to near free molecular regimes," Journal of Fluid Mechanics **584**, 337–356 (2007).

[54]D. B. Newell, F. Cabiati, J. Fischer, K. Fujii, S. G. Karshenboim, H. Margolis, E. de Mirandés, P. Mohr, F. Nez, K. Pachucki, *et al.*, "The CODATA 2017 values of h, e, k, and N_A for the revision of the SI," Metrologia **55**, L13 (2018).

[55]G. A. Radtke, *Efficient simulation of molecular gas transport for micro-and nanoscale applications*, Ph.D. thesis, Massachusetts Institute of Technology (2011).

[56]C. Cercignani and A. Daneri, "Flow of a rarefied gas between two parallel plates," Journal of Applied Physics **34**, 3509–3513 (1963).

[57]T. Ohwada, "Higher order approximation methods for the boltzmann equation," Journal of Computational Physics **139**, 1–14 (1998).

[58]D. Valougeorgis, "The friction factor of a rarefied gas flow in a circular tube," Physics of Fluids **19**, 091702 (2007).

[59]J. Meng, H. Dongari, J. Reese, and Y. Zhang, "Breakdown parameter for kinetic modeling of multiscale gas flows," Physical Review E **89**, 063305 (2014).